Electronic Supplementary Material (ESI) for Journal of Materials Chemistry A. This journal is © The Royal Society of Chemistry 2021

Electronic Supplementary Information

for

Pore-Space-Partitioned MOF Separator Promotes High-Sulfur-Loading Li-S Batteries with Intensified Rate Capability and Cycling Life

Yilong Chen,[#,a] Linjie Zhang,[#,b] Hui Pan,[c] Jindan Zhang,[a] Shengchang Xiang,[a] Zhibin Cheng,*[a,b] and Zhangjing Zhang*[a,b]

[a] *Fujian Key Laboratory of Polymer Materials, College of Chemistry and Materials Science, Fujian Normal University, Fuzhou 350007, China. Email: chengzhibin@fjnu.edu.cn, zzhang@fjnu.edu.cn*

[b] *State Key Laboratory of Structural Chemistry, Fujian Institute of Research on the Structure of Matter, Chinese Academy of Sciences, Fuzhou, Fujian, 350002, China*

[c] *Laboratory for Soft Matter and Biophysics, Department of Physics and Astronomy, KU Leuven, Leuven 3001, Belgium.*

[#] *These two authors contributed equally to this work.*

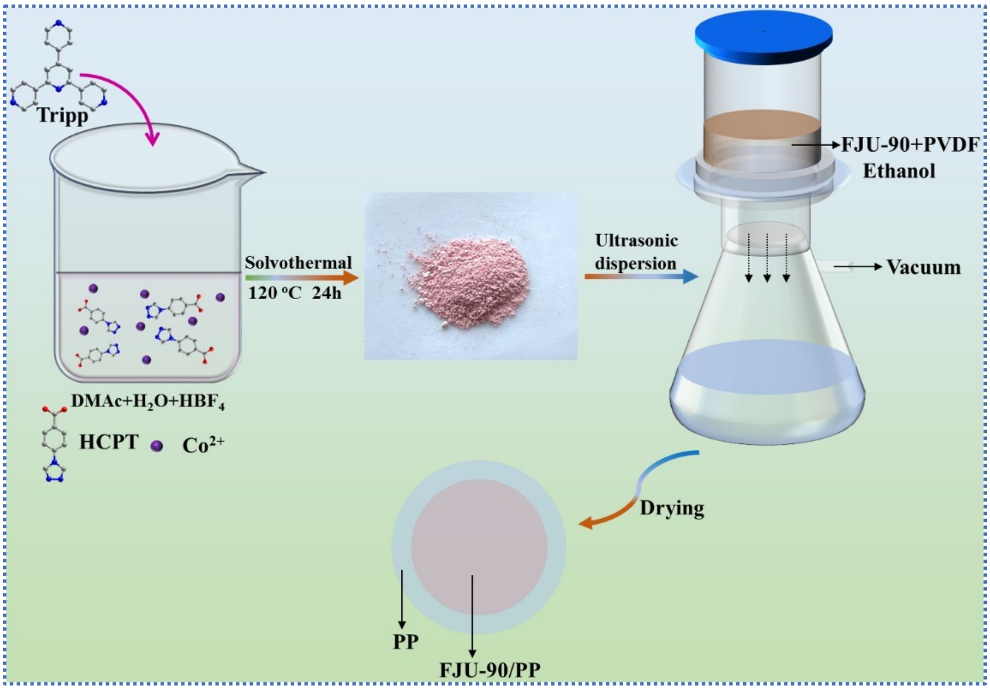

Fig. S1. Schematic illustration of the preparation of FJU-90/PP.

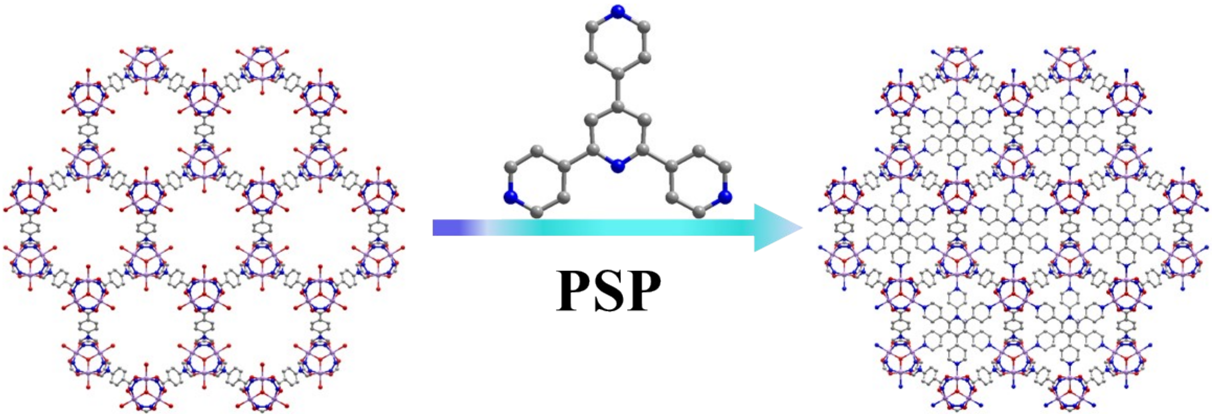

Fig. S2. View along the crystallographic *c* axis of the cylindrical channel before and after PSP partitioning.

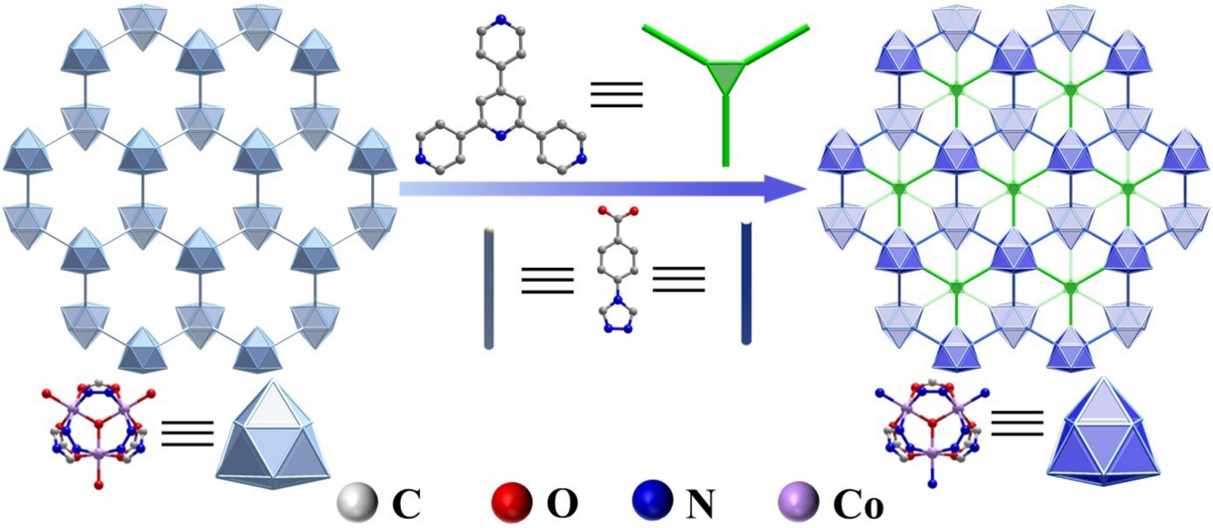

Fig. S3. Polyhedral drawing of the connected network in FJU-88 (left) and FJU-90 (right) before and PSP after partitioning.

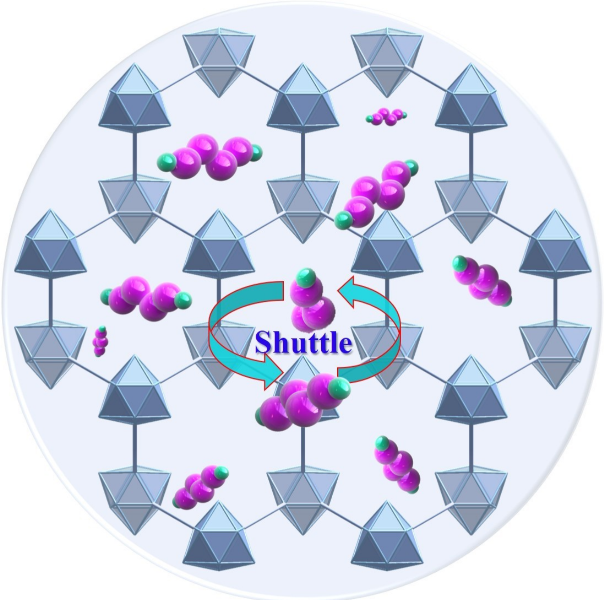

Fig. S4. Schematic diagram of the shuttle effect of the FJU-88/PP separator.

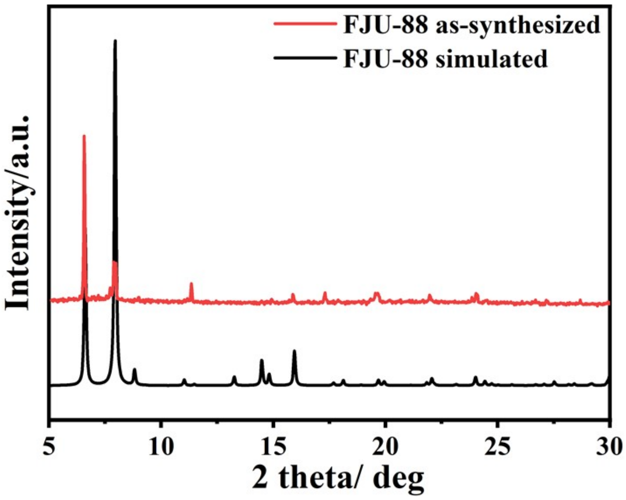

Fig. S5. XRD pattern of FJU-88.

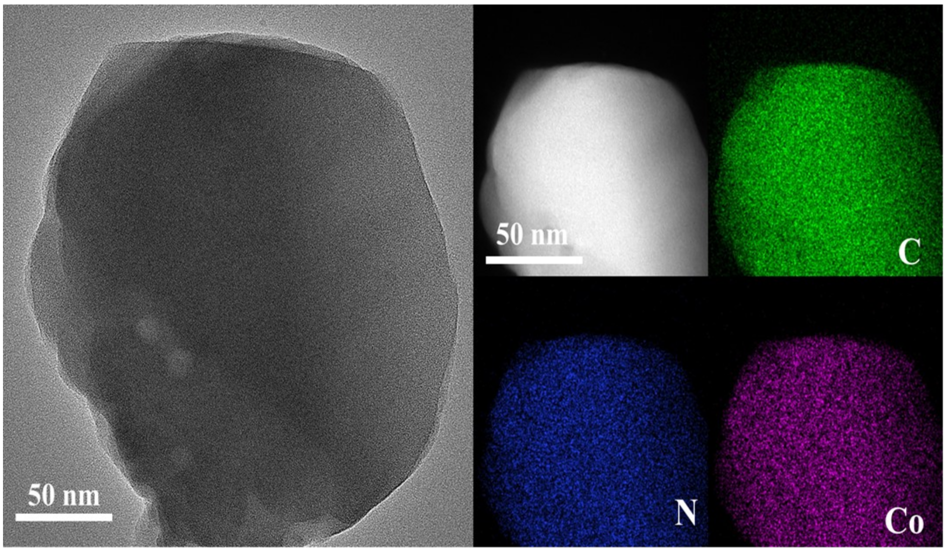

Fig. S6. HAADF-STEM image and the corresponding elemental mappings of FJU-90.

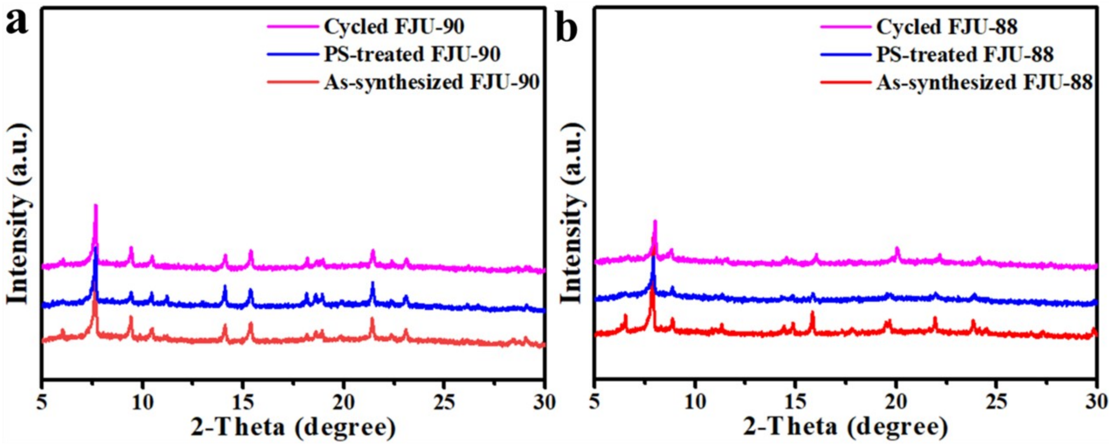

Fig. S7. XRD patterns of (a) FJU-90 and (b) FJU-88 after cycling and after soaking with polysulfides-containing electrolyte.

In order to demonstrate the stability of MOFs in Li-S battery, crystalline structures of MOFs after cycling and contacting with PS were provided. As exhibited in Fig. S7, XRD patterns of the as-synthesized MOFs are well matched with the patterns for cycled MOF and PS-treated MOF, suggesting good stability of as-prepared MOFs in Li-S battery.

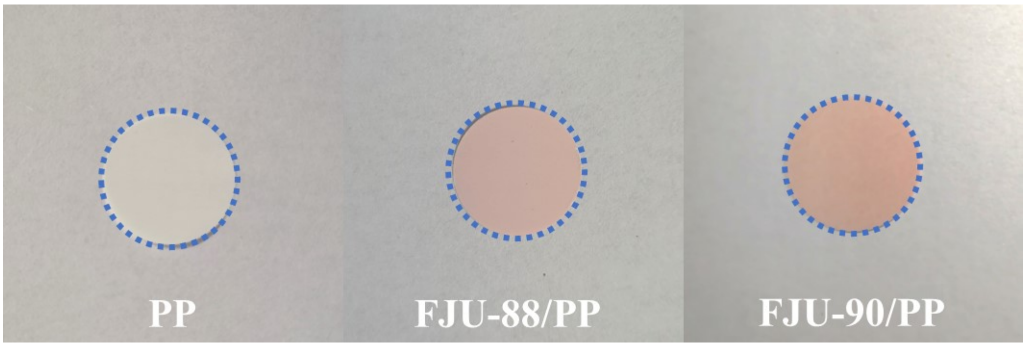

Fig. S8. Photographs of the PP, FJU-88/PP, and FJU-90/PP separators

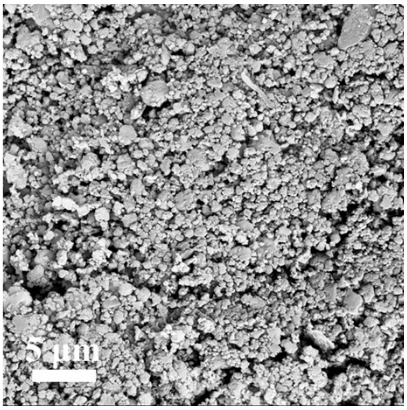

Fig. S9. Top-view SEM image for FJU-90/PP.

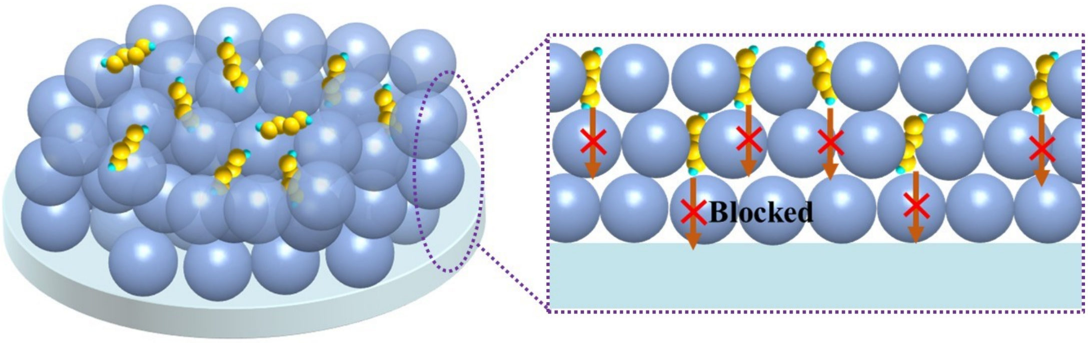

Fig. S10. Schematic of the FJU-90/PP separator for blocking the polysulfides.

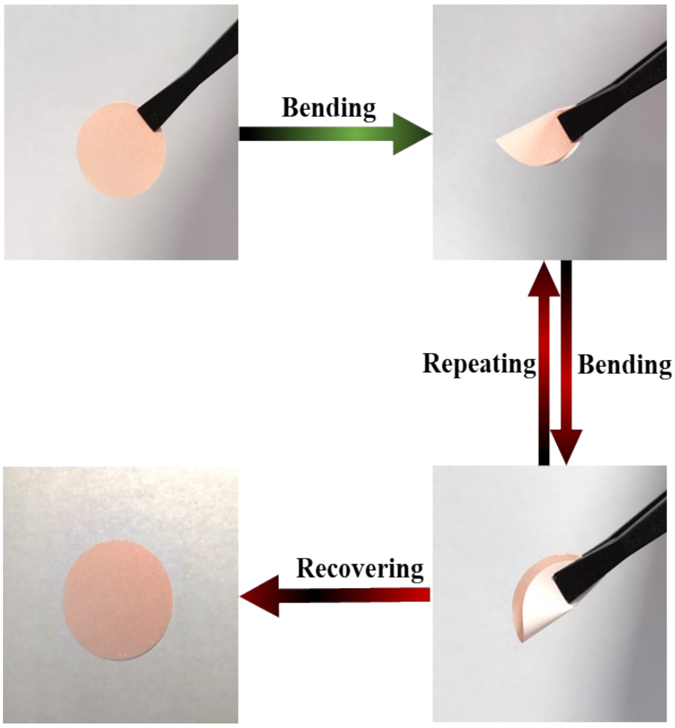

Fig. S11. FJU-90/PP separator at bending state and after recovery.

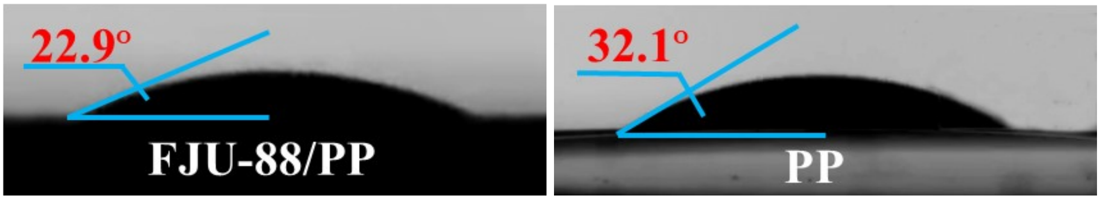

Fig. S12. Surface wetting of electrolyte droplet on FJU-88/PP and PP separators.

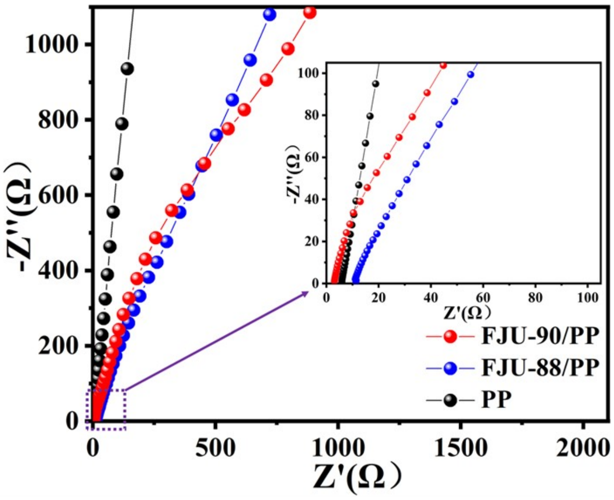

Fig. S13. Impedance plots of the batteries with different separators.

The battery was assembled by sandwiching a separator between two stainless steel blocking electrodes. The electrochemical impedance spectroscopy (EIS) was collected using an electrochemical working station at open circuit potential with constant perturbation amplitude of 5 mV in the frequency of 10 Hz-100 KHz. The Li^+ conductivity of separator was calculated using the EIS data according to equation below.

$$\sigma = L / (R_b \times A)$$

where σ is the Li^+ conductivity, mS cm^{-1}; L is the thickness of the separator, cm; R_b is the bulk resistance, Ω; and A is the area of the stainless steel electrode, cm^2.

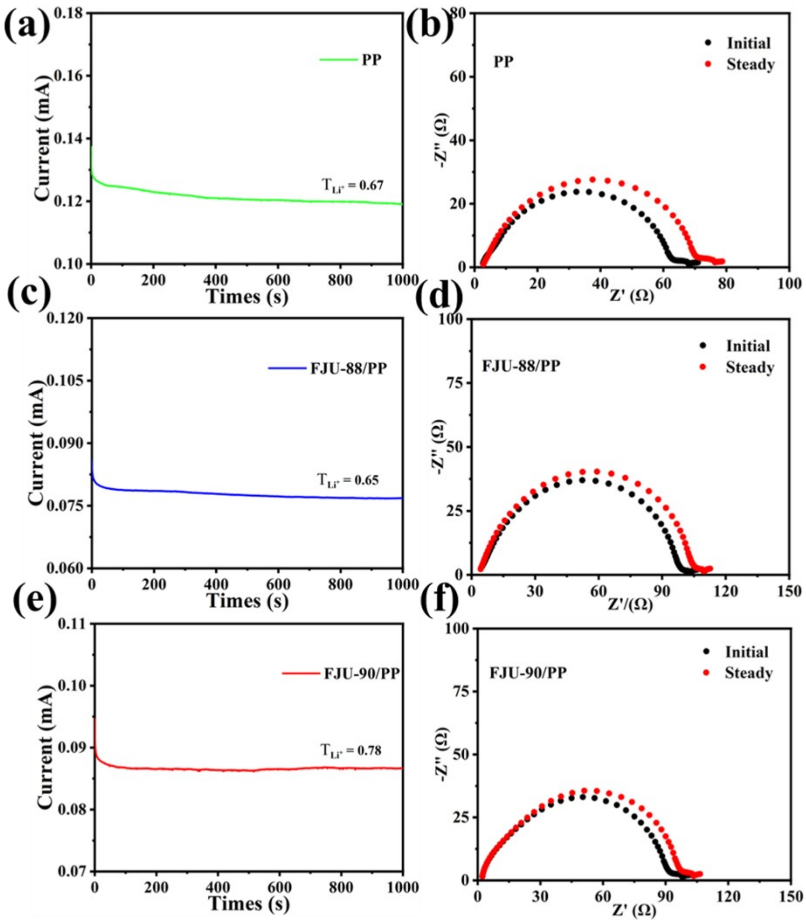

Fig. S14. (a, c, e) Variation of current with time during polarization at an applied voltage of 10 mV. EIS of the (b) Li|PP|Li, (d) Li|FJU-88/PP|Li and (f) Li|FJU-90/PP|Li symmetric cells before and after polarization.

The Li^+ transference number for different separators was determined by chronoamperometry at a constant step potential of 10 mV. Each membrane was separately sandwiched between two lithium metal electrodes in a coin type cell and Li^+ transference number was calculated according to the following equation:

$$t_{Li^+} = I_S / I_0$$

where t_{Li^+} is transference number; I_S and I_0 represent the current at the steady state and initial state, respectively.

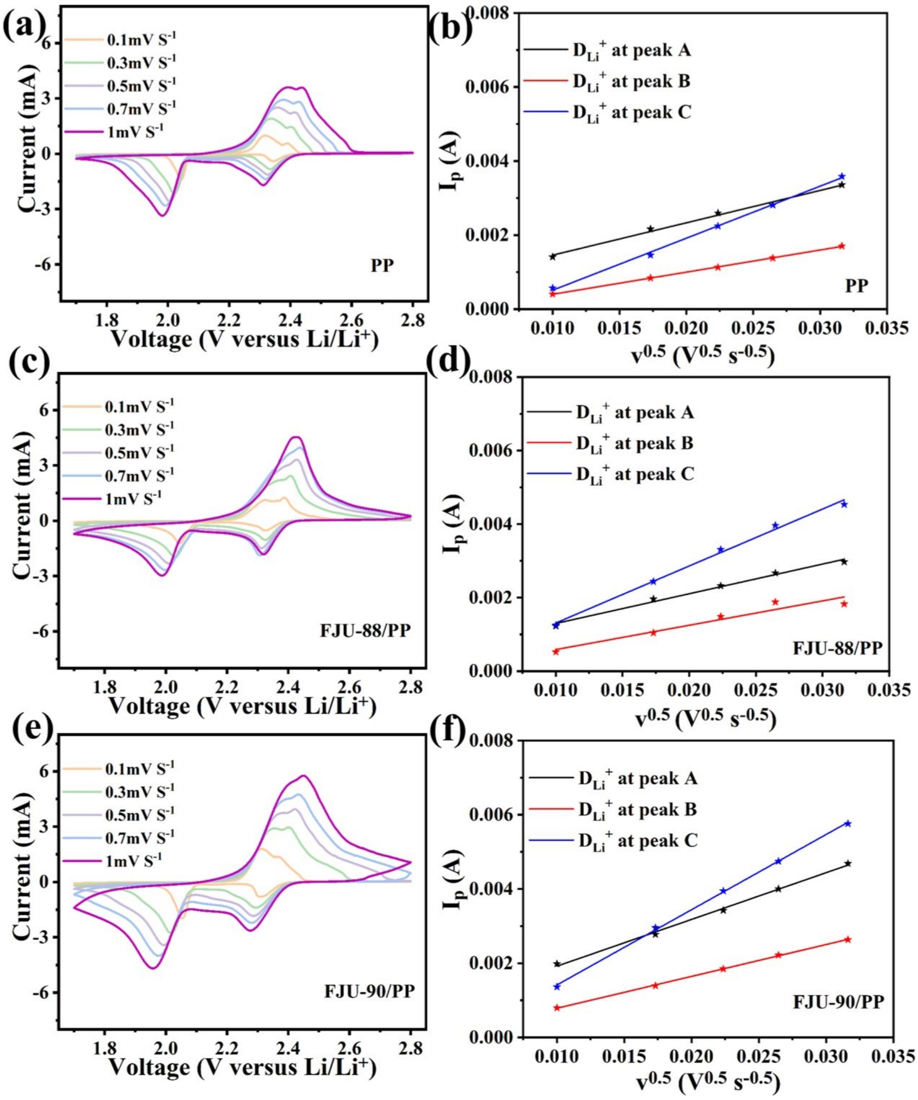

Fig. S15. Cyclic voltammograms at various voltage scan rates and corresponding linear fittings of the peak currents of Li-S batteries. (a, b) PP separator, (c, d) FJU-88/PP separator and (e, f) FJU-90/PP separator.

As shown in Fig. S15, the cathodic peaks at 1.8-2.1 V and 2.2-2.4 V are respectively labeled as A and B, while the anodic peaks at around 2.3-2.5 V as C. By adopting the Randles-Sevick equation given below[S1], the lithium ion diffusion coefficient is calculated based on the slop of the linear plot of the peak current (I_p) versus the square root of the scan rate ($V^{0.5}$).

$$I_p = 2.69 \times 10^5\ n^{1.5}\ A\ D_{Li^+}{}^{0.5}\ C_{Li}\ v^{0.5}$$

where D_{Li^+} represents lithium ion diffusion coefficient ($cm^2\ s^{-1}$), I_p is the peak current (A), n is the number of electrons involved in the reaction (n = 2 for Li-S battery), A is the area of electrode (cm^2), C_{Li} refers to the lithium ion concentration ($mol\ L^{-1}$) and v is the scanning rate ($V\ s^{-1}$).

Table S1. Lithium ion diffusion coefficients of FJU-90/PP, FJU-88/PP, and PP separators.

D_{Li^+} / cm^2 S^{-1}	**Peak A**	**Peak B**	**Peak C**
FJU-90/PP	1.0818×10^{-7}	7.3740×10^{-8}	1.7413×10^{-7}
FJU-88/PP	9.8059×10^{-8}	5.6868×10^{-8}	1.3319×10^{-8}
PP	7.5140×10^{-8}	5.1789×10^{-8}	1.2075×10^{-7}

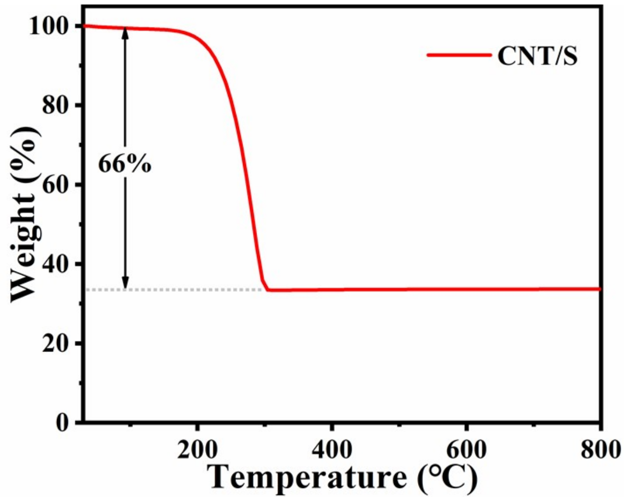

Fig. S16. TGA curve of CNT/S composite with 66 wt% sulfur loading.

CNT/S composite was prepared through a conventional melt-diffusion method. As shown in Fig. S16, a sulfur content of 66 wt% is determined for CNT/S by the weight loss of sulfur due to the evaporation.

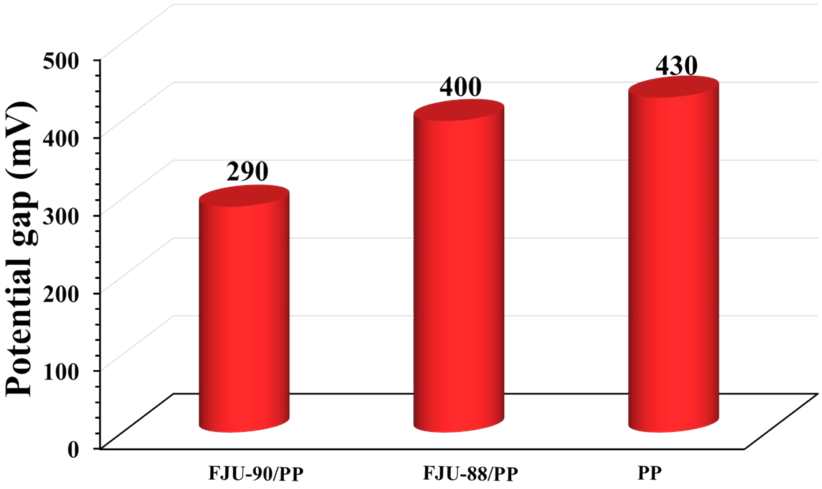

Fig. S17. Potential gaps between redox peaks obtained from CV results.

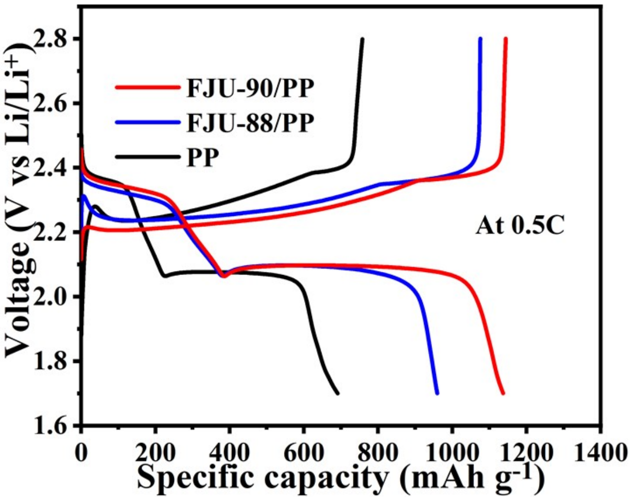

Fig. S18. Charge/discharge profiles of FJU-90/PP, FJU-88/PP and PP cells at 0.5 C, respectively.

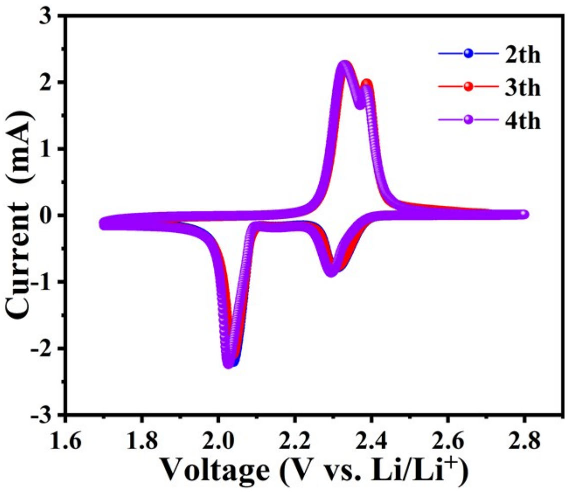

Fig. S19. CV profiles of cell with FJU-90/PP separator.

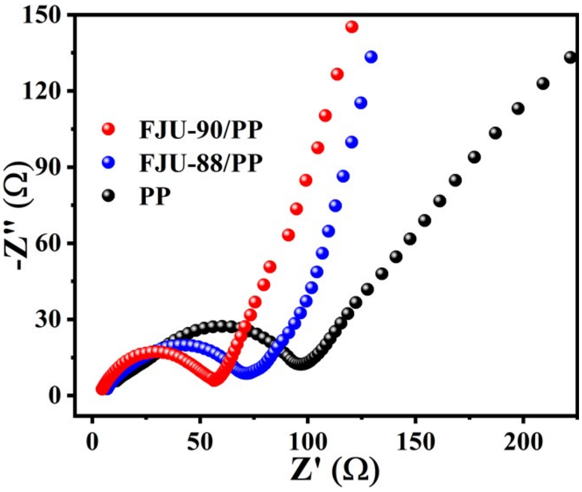

Fig. S20. EIS spectra of the cells with FJU-90/PP, FJU-88/PP, and PP separators.

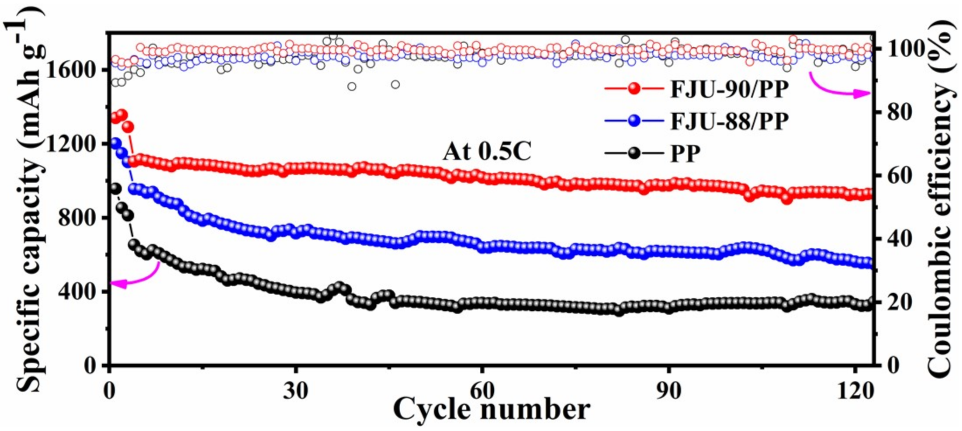

Fig. S21. Cyclic performances of FJU-90/PP, FJU-88/PP and PP cellsat 0.5 C.

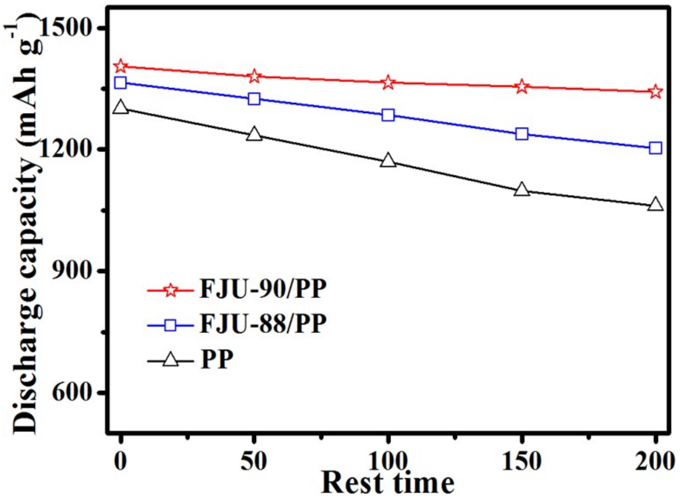

Fig. S22. Self-discharge behavior of FJU-90/PP, FJU-88/PP and PP. The cells were tested with a current density of 0.05 C.

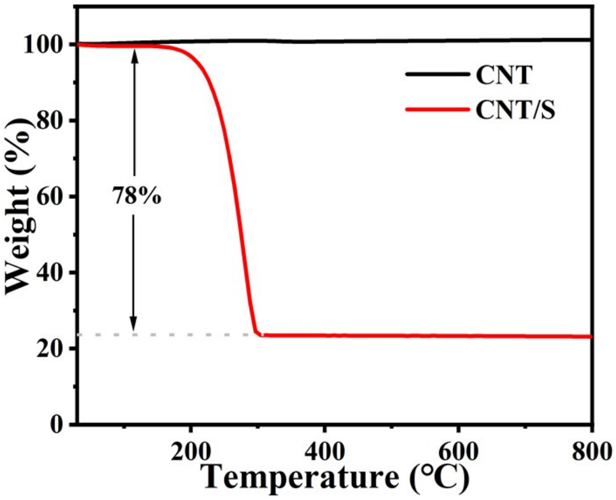

Fig. S23. TGA curve for CNT/S composite with 78 wt% sulfur content.

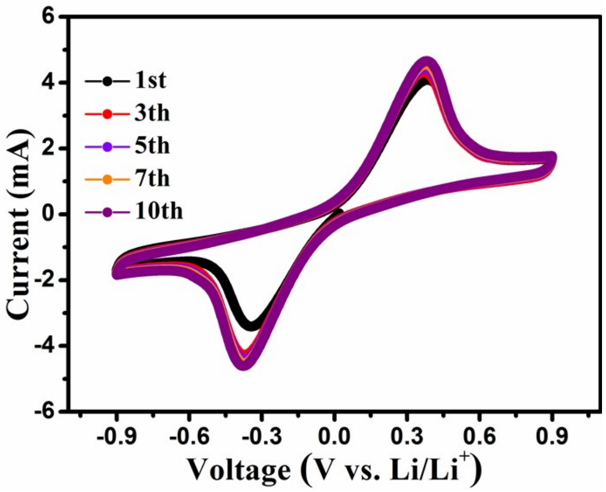

Fig. S24. CV curves of symmetric cells at scan rate of 10 mV s^{-1} for the FJU-90 electrodes.

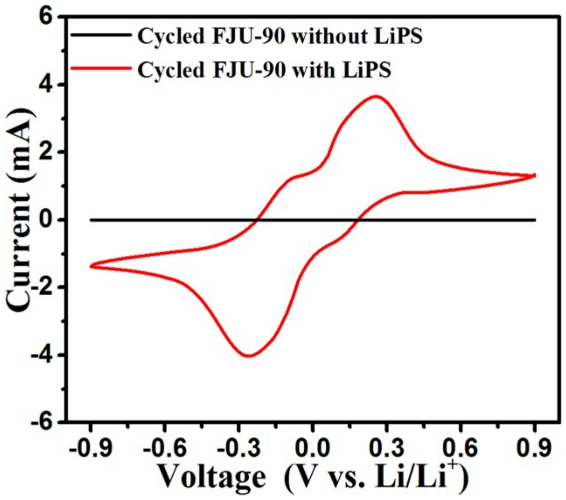

Fig. S25. CV curves of symmetric cells with cycled FJU-90.

We have performed more experiments for demonstrating that the solid deposits on modified separator could not block the catalytic process. The FJU-90/PP cell in the discharge state was disassembled after rate performance test, and the separator modified layer was collected for symmetrical cell measurements. As shown in Fig. S25, the cycled FJU-90 still exhibits large redox current, implying well catalytic effect of cycled FJU-90 on the conversion of PS. The result clearly corroborated that the solid deposit could be reutilized and not block the catalytic process.

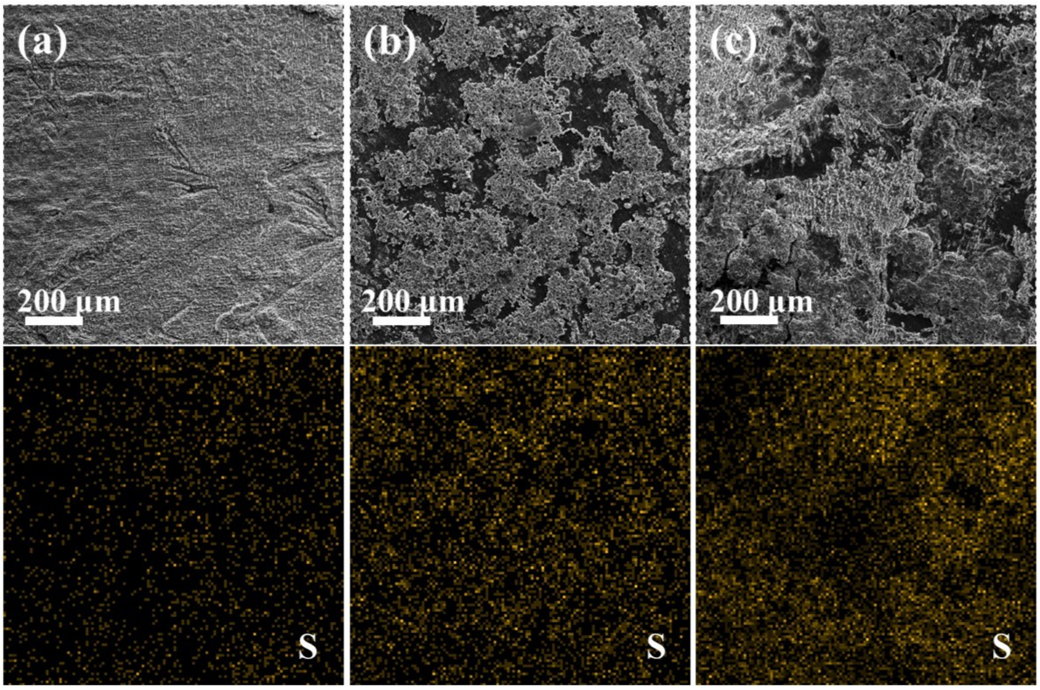

Fig. S26. SEM images and corresponding EDS elemental mapping of the cycled lithium foils disassembled from cells run with (a) FJU-90/PP, (b) FJU-88/PP and (c) PP separator.

The cells were disassembled and inspected after cycling. As shown in Fig. S26, it can be seen from the SEM images that the surface of the Li anode in the cell with FJU-90/PP remains relatively smooth and flat after cycling. In sharp contrast, the surfaces of Li anode in the cells with FJU-88/PP and PP after cycling are rough with obvious lithium dendrite growth. Besides, as revealed by energy-dispersive X-ray spectroscopy (EDS) analyses, the sulfur content of the Li surface for FJU-90/PP cell is 2.79 at%, which is smaller than those of Li surfaces for FJU-88/PP (7.96 at%) and PP (8.37 at%) cells. The reason for these difference may be related to the more favorable porous structure of FJU-90 with a pore size distribution narrowly concentrated at ~9 Å, which not only benefits for inhibiting the diffusion of polysulfides, but also formation of uniform lithium ion flux to achieve stable lithium electrodeposition.

Table S2. Electrochemical properties of various functional separators in Li-S batteries.

Coating	Surfur content (wt%)	Initial capacity (mAh g^{-1})	Rate (C)	Capacity deacy (%)	Reference
Black Phosphorus	66	930	0.5	0.14(100th)	S2
GO	63	920	0.1	0.23(500th)	S3
B-rGO	70	1227.8	0.1	0.15(300th)	S4
$Li_4Ti_5O_{12}$/G	60	1408	0.3	0.15(300th)	S5
BN-Carbon	60	1018.5	0.5	0.09(250th)	S6
Nafion	50	800	1	0.08(500th)	S7
MoS_2	65	808	0.5	0.083(600th)	S1
CNTs/NCQD	60	1330.8	0.5	0.10(500th)	S8
Co_9S_8	70	869	1	0.039(1000th)	S9
MoP/rGO	77	880	0.5	0.045(300th)	S10
Porous graphene	63	1165	0.5	0.16(150th)	S11
SnS_2	70	1300	0.2	0.15(150th)	S12
$BaTiO_3$	60	1122.1	0.1	0.34(50th)	S13
CNT@ZIF	70	1588.4	0.2	0.45(100th)	S14
Super P	63	1025	0.6	0.05(500th)	S15
LDH/graphene	63	851	2	0.06(1000th)	S16
Graphene	70	890.3	0.9	0.064(500th)	S17
CoP nanospheres	70	928	1	0.078(500th)	S18
$Ti_3C_2T_x$ MXene	68	811.4	0.5	0.062(500th)	S19
ZBCP layer	70	1272	0.25	0.21(200th)	S20
Super P/RP	65	890	1	0.18(500th)	S21
Zn-HKUST-1@GO	70	1118	1	0.041(1000th)	S22
Cu-HKUST-1@GO	70	1207	1	0.019(1500th)	S23
Mn-BTC/PP	65	1450	0.1	0. 3(80th)	S24
HKUST-1/GF	70	1032	0.25	0.27(300th)	S25
ZIF-8/GF	70	989	0.25	0.198(300h)	S25
ZIF-7/GF	70	1025	0.25	0.186(300th)	S25

Y-FTZB/GF	70	1101	0.25	0.165(300th)	S25
$Ni_3(HITP)_2$/PP	70	1055	0.5	0.07(200th)	S26
PSS@HKUST-1	70	1243	0.5	0.079(500th)	S27
Ni-MOF/CNT/PE	60	1358	0.2	0.042(300th)	S28
UiO-66-S/Nafion	70.5	1127.4	0.1	0.109(200th)	S29
aMIL-88B	75	953	1	0.045(500th)	S30
MOF@PVDF-HFP	87	1269	0.1	0.13(200th)	S31
Ce-MOF-2/CNT	88	993.5	0.1	0.054(200th)	S32
UiO-66/PP	65	1032	0.5	0.086(500th)	S33
PVDF/Mg-MOF-74	70	1383.1	0.1	0.14(200th)	S34
Cu_2(CuTCPP)/PP	64	850	1	0.032(900th)	S35
UiO-66-SO_3	70	1020	0.5	0.056(500th)	S36
ZIF-67/GO/PP	70	616.9	1	0.1(200th)	S37
MIL-125-Ti/PP	70	1218.3	0.2	0.2(200th)	S38
MOF-PAN/rGO-PAN	-	1116	1	0.17(100th)	S39
Ms-9.0-NSP/PP	70	1316	0.5	0.028(500th)	S40
UiO-66/PP	67	1147.4	0.5	0.08(200th)	S41
HKUST-1@PVDF-HFP	69.1	1163.7	0.5	0.08（700th）	S42
NH_2-UiO-66/Ce-BTB	-	1161.2	0.1	1.35(30th)	S43
FJU-90/PP	**66**	**1045**	**1**	**0.042(500th)**	**This work**
	78	**1071**	**0.5**	**0.091(300th)**	

References

S1. Z. A. Ghazi, X. He, A. M. Khattak, N. A. Khan, B. Liang, A. Iqbal, J. Wang, H. Sin, L. Li and Z. Tang, *Adv. Mater.*, 2017, **29**, 1606817.

S2. J. Sun, Y. Sun, M. Pasta, G. Zhou, Y. Li, W. Liu, F. Xiong and Y. Cui, *Adv. Mater.*, 2016, **28**, 9797-9803.

S3. J. Q. Huang, T. Z. Zhuang, Q. Zhang, H. J. Peng, C. M. Chen and F. We, *ACS Nano*, 2015, **9**, 3002-3011.

S4. F. Wu, J. Qian, R. Chen, Y. Ye, Z. Sun, Y. Xing and L. Li, *J. Mater. Chem. A*, 2016, **4**, 17033-17041.

S5. Y. Zhao, M. Liu, W. Lv, Y. B. He, C. Wang, Q. Yun, B. Li, F. Kang and Q. H. Yang, *Nano Energy*, 2016, **30**, 1-8.

S6. P. J. H. Kim, J. Seo, K. Fu, J. Choi, Z. Liu, J. Kwon, L. Hu and U. Paik, *NPG Asia Mater.*, 2017, **9**, e375-e375.

S7. J. Q. Huang, Q. Zhang, H. J. Peng, X. Y. Liu, W. Z. Qian and F. Wei, *Energy Environ. Sci.*, 2014, **7**, 347-353.

S8. Y. Pang, J. Wei, Y. Wang and Y. Xia, *Adv. Energy Mater.*, 2018, **8**, 1702288.

S9. J. He, Y. Chen and A. Manthiram, *Energy Environ. Sci.*, 2018, **11**, 2560-2568.

S10. M. Li, C. Wang, L. Miao, J. Xiang, T. Wang, K. Yuan, J. Chen and Y. Huang, *J. Mater. Chem. A*, 2018, **6**, 5862-5869.

S11. P. Y. Zhai, H. J. Peng, X. B. Cheng, L. Zhu, J. Q. Huang, W. C. Zhu and Q. Zhang, *Energy Storage Mater.* , 2017, **7**, 56-63.

S12. B. Moorthy, S. Kwon, J. H. Kim, P. Ragupathy, H. M. Lee and D. K. Kim, *Nanoscale Horiz.*, 2019, **4**, 214-222.

S13. T. Yim, S. H. Han, N. H. Park, M.-S. Park, J. H. Lee, J. Shin, J. W. Choi, Y. Jung, Y. N. Jo, J. S. Yu and K. J. Kim, *Adv. Funct. Mater.*, 2016, **26**, 7817-7823.

S14. F. Wu, S. Zhao, L. Chen, Y. Lu, Y. Su, Y. Jia, L. Bao, J. Wang, S. Chen and R. Chen, *Energy Storage Mater.*, 2018, **14**, 383-391.

S15. H. Wang, W. Zhang, H. Liu and Z. Guo, *Angew. Chem. Int. Ed.*, 2016, **55**, 3992-3996.

S16. H. J. Peng, Z. W. Zhang, J. Q. Huang, G. Zhang, J. Xie, W. T. Xu, J. L. Shi, X. Chen, X. B. Cheng and Q. Zhang, *Adv. Mater.*, 2016, **28**, 9551-9558.

S17. G. Zhou, L. Li, D. W. Wang, X. Y. Shan, S. Pei, F. Li and H. M. Cheng, *Adv. Mater.*, 2015, **27**, 641-647.

S18. X. Chen, X. Ding, C. Wang, Z. Feng, L. Xu, X. Gao, Y. Zhai and D. Wang, *Nanoscale*, 2018, **10**, 13694-13701.

S19. J. Song, D. Su, X. Xie, X. Guo, W. Bao, G. Shao and G. Wang, *ACS Appl. Mater. Interfaces*, 2016, **8**, 29427-29433.

S20. J. K. Huang, M. Li, Y. Wan, S. Dey, M. Ostwal, D. Zhang, C. W. Yang, C. J. Su, U. S. Jeng, J. Ming, A. Amassian, Z. Lai, Y. Han, S. Li and L. J. Li, *ACS Nano*, 2018, **12**, 836-843.

S21. Z. Wang, M. Feng, H. Sun, G. Li, Q. Fu, H. Li, J. Liu, L. Sun, A. Mauger, C. M. Julien, H. Xie and Z. Chen, *Nano Energy*, 2019, **59**, 390-398.

S22. S. Bai, K. Zhu, S. Wu, Y. Wang, J. Yi, M. Ishida and H. Zhou, *J. Mater. Chem. A*, 2016, **4**, 16812-16817.

S23. S. Bai, X. Liu, K. Zhu, S. Wu and H. Zhou, *Nat. Energy*, 2016, **1**, 16094

S24. S. Suriyakumar, M. Kanagaraj, M. Kathiresan, N. Angulakshmi, S. Thomas and A. M. Stephan, *Electrochim. Acta*, 2018, **265**, 151-159.

S25. M. Li, Y. Wan, J. K. Huang, A. H. Assen, C. E. Hsiung, H. Jiang, Y. Han, M. Eddaoudi, Z. Lai, J. Ming and L. J. Li, *ACS Energy Lett.*, 2017, **2**, 2362-2367.

S26. Y. Zang, F. Pei, J. Huang, Z. Fu, G. Xu and X. Fang, *Adv. Energy Mater.*, 2018, **8**, 1802052.

S27. Y. Guo, M. Sun, H. Liang, W. Ying, X. Zeng, Y. Ying, S. Zhou, C. Liang, Z. Lin and X. Peng, *ACS Appl. Mater. Interfaces*, 2018, **10**, 30451-30459.

S28. D. H. Lee, J. H. Ahn, M.-S. Park, A. Eftekhari and D.-W. Kim, *Electrochim. Acta*, 2018, **283**, 1291-1299.

S29. S. Kim, J. S. Yeon, R. Kim, K. Choi and H. S. Park, *J. Mater. Chem. A*, 2018, **6**, 24971-24978.

S30. X. Zhang, G. Li, Y. Zhang, D. Luo, A. Yu, X. Wang and Z. Chen, *Nano Energy*, 2021, **86**.

S31. Y. He, Z. Chang, S. Wu, Y. Qiao, S. Bai, K. Jiang, P. He and H. Zhou, *Adv. Energy Mater.*, 2018, **8**, 1802130.

S32. X. J. Hong, C. L. Song, Y. Yang, H. C. Tan, G. H. Li, Y. P. Cai and H. Wang, *ACS Nano*, 2019, **13**, 1923-1931.

S33. Y. Fan, Z. Niu, F. Zhang, R. Zhang, Y. Zhao and G. Lu, *ACS Omega*, 2019, **4**, 10328-10335.

S34. D. D. Han, Z. Wang, G. Pan and X. Gao, *ACS Appl. Mater. Interfaces*, 2019, **11**, 18427-18435.

S35. M. Tian, F. Pei, M. Yao, Z. Fu, L. Lin, G. Wu, G. Xu, H. Kitagawa and X. Fang, *Energy Storage Mater.*, 2018, **21**, 14-21.

S36. Z. Wang, W. Huang, J. Hua, Y. Wang, H. Yi, W. Zhao, Q. Zhao, H. Jia, B. Fei and F. Pan, *Small Methods*, 2020, **4**, 2000082.

S37. B. Liu, M. Taheri, J. Torres, Z. Fusco, T. Lu, Y. Liu, T. Tsuzuki, G. Yu and A. Tricoli, *ACS Nano*, 2020, **14**, 13852-13864.

S38. C. Qi, L. Xu, J. Wang, H. Li, C. Zhao, L. Wang and T. Liu, *ACS Sustainable Chem. Eng.*, 2020, **8**, 12968-12975.

S39. C. Zhou, Q. He, Z. Li, J. Meng, X. Hong, Y. Li, Y. Zhao, X. Xu and L. Mai, *Chem. Eng. J.*, 2020, **395**, 124979.

S40. Z. Chang, Y. Qiao, J. Wang, H. Deng, P. He and H. Zhou, *Energy Storage Mater.*, 2020, **25**, 164-171.

S41. J. Han, S. Gao, R. Wang, K. Wang, M. Jiang, J. Yan, Q. Jin and K. Jiang, *J. Mater. Chem. A*, 2020, **8**, 6661-6669.

S42. G. Gao, Y. Wang, H. Zhu, Y. Chen, R. Yang, C. Jiang, H. Ma and Y. Lan, *Adv. Sci.*, 2020, **7**, 2002190.

S43. G. Gao, Y. Wang, S. Wang, R. Yang, Y. Chen, Y. Zhang, C. Jiang, M. Wei, H. Ma and Y. Lan, *Angew. Chem. Int. Ed.*, 2021, **60**, 2-10.